Korean J. Chem. Eng., 37(12), 2232-2247 (2020)
DOI: 10.1007/s11814-020-0641-z

pISSN: 0256-1115
eISSN: 1975-7220

Robust siloxane/graphene oxide thin film membranes: Siloxane size adjustment for improved separation performance and flux recovery

Solmaz Valizadeh*, Leila Naji*,†, and Mohammad Karimi**

*Department of Chemistry, AmirKabir University of Technology, 424 Hafez Avenue, Tehran P. O. Box: 15875-4413, Iran
**Department of Textile Engineering, AmirKabir University of Technology,
424 Hafez Avenue, Tehran P. O. Box: 15875-4413, Iran
(*Received 25 December 2019 • Revised 2 July 2020 • Accepted 19 July 2020*)

Abstract−Siloxane/graphene oxide (GO) nanocomposites were synthesized by hydrolysis and condensation of tetraethyl orthosilicate in the presence of GO nanosheets through a sol-gel process. The influence of synthesis parameters on the properties of the siloxane/GO samples was studied and their structural, morphological and physicochemical characteristics were compared using various techniques. Polyether sulfone-supported GO and siloxane/GO thin film membranes were prepared using a pressure-assisted self-assembly method using a dead-end cell, and their separation performance and antifouling ability were evaluated. Siloxane/GOs appeared to have higher interlayer spacing, higher zeta potential and thus higher dispersion stability in aqueous media compared to GO. This gave rise to slower and more uniform sedimentation of the siloxane/GOs during the filtration process and formation of thin film membranes possessing denser and smoother morphology. The porosity, mean pore radius, water contact angle and pure water flux of the prepared membranes were compared. The separation performance of the prepared membranes to remove methylene blue (MB) and penicillin G-procaine (PG-P) from water was evaluated as a function of used GO solution concentration. The antifouling ability of membranes was studied by determining reversible fouling (R_r), irreversible fouling (R_{ir}) resistances and flux recovery ratio (FRR). The siloxane/GO thin film membranes containing larger siloxane network exhibited the highest rejection percentage for MB (~99%) and PG-P (~88%), which were about 40% and 90% higher than that achieved for GO thin film membranes, while the water flux remained as high as 78.1 $l \cdot m^{-2}h^{-1}$. Furthermore, these membranes exhibited the highest chlorine resistance, stability under ultrasonication, FRR (89%) and R_r (57%) values, implying higher chemical and mechanical stability, flux recovery capacity and antifouling ability.

Keywords: Membrane Separation, Graphene Oxide Thin Film Membranes, Siloxane Network, Penicillin G-procaine, Antifouling Characteristics

INTRODUCTION

Nanofiltration membranes are able to remove dissolved chemical constituents such as ionic solutes from feed stream as a result of steric, dielectric and Donnan exclusion and also by adsorption to the membrane surface [1]. These membranes, which provide higher water permeability and operate at lower hydraulic pressures, compared to reverse osmosis membrane, have been applied in various industrial applications such as drinking water production and wastewater treatment [2,3] to remove organic pollutants such as dyes and pharmaceuticals [4]. Graphene oxide (GO) membranes have attracted a great deal of attention in nanofiltration processes [5], due to their higher chemical stability, higher water permeability, easier manufacturing process and lower production cost [6,7] compared to conventional polymeric membranes. GO nanosheets consist of a hexagonal ring-based carbon network having both sp^2- and sp^3-hybridized carbon atoms and a great number of oxygen-containing functional groups covalently bonded to graphene basal plane and edges. These functional groups enable GO to be easily functionalized and simply be dispersed in water and other polar solvents, providing homogeneous and stable suspensions [8]. GO nanosheets can be reunited into large-area membranes with interlocking structure and controlled thickness using vacuum filtration, spin coating and drop-casting methods [9,10]. The oxidation degree of GO is often evaluated by C/O ratio in structure [11,12]. The oxygenated functional groups provide empty spaces between GO nanosheets and form a network of nanocapillaries within GO membranes, which allows water molecules to pass through freely while other liquids and gases are completely blocked [9,13]. It has been reported that water permeate across the GO thin film membrane is 10^{10} times higher than helium [6,14]. Researchers have found that decreasing membrane thickness [15] and introducing in-plane nanopores into GO nanosheets can considerably improve membrane permeability, while membrane selectivity is greatly influenced by the level of laminar order of nanochannels - a more ordered structure shows higher selectivity [15]. The structure of GO membranes can be adjusted by the self-assembly rate of GO nanosheets through vacuum filtration; a slower rate provides more-ordered laminar structure, leading to higher separation performance in terms of water flux and salt rejection. The selective sieving behavior of GO membranes towards different species has been described based on the mechanism of size effect, coordination effect, electrostatic

†To whom correspondence should be addressed.
E-mail: leilanaji@aut.ac.ir

and cation-π interactions [16].

The stability of interlayer spacing of GO nanosheets and their lamellar structure are of great significance to the separation performance and antifouling properties of GO membranes. However, the nanocapillaries which form interlayer spacing are metastable and they might collapse through drying and post-treatments processes [17]. This can greatly be avoided by intercalating metal nanoparticles [19], inorganic nanoparticles [20], organic molecules [10] and polymers [21] between GO nanosheets through physical and chemical methods. This can also improve the mechanical stability of GO membranes, which is of a crucial importance in their practical applications [22]. For instance, Park et al. [23] showed that the mechanical stability of GO membranes can be significantly enhanced (~200%) by interacting negatively charged oxygenated functional groups on the GO nanosheets with a small amount (less than 1%) of Mg^{2+} and Ca^{2+} ions. Jia et al. [24] showed that chemical crosslinking of GO nanosheets by diamines could hinder the extreme swelling of the GO-based membranes through dialysis process. The prepared membranes showed high selectivity factor for separation of K^{+}/Mg^{2+} ions. The modification of GO by tetraethyl orthosilicate (TEOS) as a silane precursor has been reported by Zhang et al. [25], who found SiO_2 nanoparticles are covalently grafted to GO nanosheets and can improve the thermal stability of GO. In another work [26], silica/reduced GO (r-GO) composites were prepared by sol-gel reaction of TEOS in the presence of GO followed by reduction of GO to r-GO. The resulting composite was applied as an efficient adsorbent for the removal of organic contaminant from water. The preparation of silica-crosslinked GO-based thin film membranes and their ability to remove neutral organic molecules from water has also been reported [27,28]. GO membranes were first prepared by the vacuum filtration method and then soaked in a saturated solution of Na_2SiO_3, followed by immersing in an acidic solution for further stabilization.

Despite the abundant studies on GO thin film membranes for wastewater treatment processes, they are unstable in water and easily detached from the polymeric support membrane due to their hydrophilic nature. This results in variations of membrane permeance and water flux during the separation process and limits their applications in aqueous medium. It has been shown that the stability of GO thin film membranes in water can be improved by adjusting the oxidation degree of GO through synthesis process [28], and by building interlayer crosslinking between GO nanosheets [29] to control the swelling level of nanochannels. However, the fabrication of GO membranes possessing a well-defined interlayer spacing showing high stabilities in water has still remained challenging.

In this study, we demonstrate the use of siloxane networks as an efficient crosslinker to fabricate GO thin film membranes possessing controllable interlayer spacing with extraordinary stability in water. Siloxane/GO nanocomposites were prepared by hydrolysis and condensation of TEOS in the presence of GO nanosheets using a sol-gel process and then exploited in the fabrication of polyether sulfone (PES) supported siloxane/GO thin film membranes by the vacuum filtration method using a dead-end cell. The size of the siloxane network and the interlayer spacing of GO nanosheets were adjusted by controlling the rate of hydrolysis and condensation of the sol-gel process, via altering the catalyst concentration and temperature of the reaction. Despite the significant influence of the sol-gel synthesis parameters on the size and surface charge of the siloxane networks, there is a lack of such studies aiming to control the interlayer spacing of GO nanosheets and the separation performance of the corresponding GO membranes through changing sol-gel reaction parameters. Moreover, to understand the separation mechanism of GO membranes, the separation capability of the prepared GO membranes was evaluated in a pressurized membrane system using Penicillin G-procaine (PG-P) and Methylene blue (MB). The separation performance of the nanofiltration membranes can be interpreted in terms of size and/or charge exclusion mechanisms [30]. Therefore, to find which mechanism has a higher contribution, the neutral species of PG-P and the positively charged species of MB were selected. The chemical structure and the molecular weight of PG-P and MB are compared in Table S1 (see Supporting Information). As can be seen, the molecular weight and the size of PG-P are higher than those of MB.

MATERIALS AND METHODS

1. Materials

Polyether sulfone (PES) support membrane with pore size of 0.2 μm was purchased from Sterlitech Company. Tris hydroxymethyl aminomethane, dopamine, graphite powder with a mean particle size less than 50 μm and bovine serum albumin (BSA) were supplied by Merck Company. Analytical grade ethanol (EtOH), sodium nitrate ($NaNO_3$), potassium permanganate ($KMnO_4$), sulfuric acid (H_2SO_4, 98%), hydrochloric acid (HCl, 36%), hydrogen peroxide (H_2O_2, 30%), methylene blue (MB) and tetraethyl orthosilicate (TEOS) were purchased from Sigma Aldrich and Penicillin G procaine (PG-P) were obtained from Shigiazhuang Co.

2. Synthesis of GO

A modified Hummers method was employed for synthesis of GO [31]. Briefly, H_2SO_4 (8 mL, 98%) was added to graphite (0.35 g) and $NaNO_3$ (0.175 g) in 250 mL flask at room temperature. The mixture was stirred for 2 h using a magnetic stirrer and then $KMnO_4$ powder (1.05 g) was slowly added to flask at 0 °C (in an ice bath). The mixture was vigorously stirred below 10 °C for 1 h, and then heated to 35 °C and stirred for 12 h. By adding 200 mL distilled water, the temperature was raised to 98 °C for 15 min and then the reaction was terminated by addition of 12 mL aqueous solution of H_2O_2 (30%). The mixture was filtrated and washed with hydrochloric acid (5%) to remove SO_4^{2-} ions. The product was repeatedly washed with deionized (DI) water until pH reached to 7. The obtained brown dispersion was centrifuged at 1,000 rmp for 10 min to remove unreacted graphite. Finally, the obtained GO was dried under vacuum at 60 °C for 24 h and stored at room temperature.

3. Modification of GO by TEOS

Siloxane/GO was synthesized by hydrolysis of TEOS in the presence of GO. Two types of siloxane/GO samples were prepared by altering the reaction parameters and the order of steps. In the first method, GO powder (100 mg) was dispersed in 20 mL aqueous ammonia solution (25% w/w) by ultrasonic treatment for 2 h. Under fast stirring, the prepared GO suspension was added to 200 mL mixture of water-ethanol (1 : 1) and excess amount of ammonium

hydroxide (5 mL) was added to the mixture for adjusting hydrolysis rate. Then, 20 mL ethanol with 1 mL TEOS was dropwise added to the mixture under fast stirring. The mixture was stirred overnight and then washed with DI water and centrifuged at 2,000 rpm for 5 min. The obtained product was dispersed in 40 mL DI water and named as GO-T1 solution. In the second method, GO powder (100 mg) was dispersed in 20 mL of DI water by ultrasonic treatment (2 h) and no ammonium hydroxide was added in this step. Under fast stirring, the prepared GO suspension was added to 200 mL mixture of water-ethanol (1 : 1). Afterwards, 20 mL ethanol with 1 mL TEOS was dropwise added to the mixture under fast stirring same as the first method. Unlike the first method, the temperature of mixture was raised to 40 °C and ammonium hydroxide solution (5 mL) was added. The reaction mixture was further stirred overnight and washed with DI water and centrifuged at 2,000 rpm for 5 min. The obtained sample was dispersed in 40 mL DI water and the solution was named as GO-T2.

4. Physicochemical Characterization of GO Samples

The chemical structure of the prepared GO and siloxane/GO samples was compared by Fourier transformed infrared (FT-IR) spectroscopy in wavenumber range of 380-4,000 cm^{-1} in transmittance mode by a Bruker alpha spectrophotometer. KBr was used as reference and similar weight of samples was applied for preparation of sample pellets for comparison reasons. The crystalline structure of the synthesized samples was analyzed by an X-ray powder diffractometer (XRD) (EQuniox 3000) using Cu radiation under a scan rate of 0.5°/min and incident wavelength of 0.1549056 nm (Cu Kα). The size of crystallites was estimated using Scherrer equation shown in Eq. (1) [32]:

$$L = \frac{K\lambda}{\beta \cos\theta} \quad (1)$$

where L is the mean size of the crystallites; K is a dimensionless shape factor with a typical value of about 0.9; λ is the X-ray wavelength (A°); β is the line broadening at full width half maximum (FWHM) in radians and θ is the Bragg angle in degrees. Raman spectra were recorded using a Teksan-Takram spectrometer with 532 nm wavelength incident laser light. The first-order Raman spectra were fitted to five bonds contribution using Gaussian function in the range of 1,000-2,000 cm^{-1} by the *Origin* 9.1 software and the second-order spectrum in the range of 2,300-3,500 cm^{-1} was split into four Lorentzian contributions [33]. TEM images were acquired on a ZEISS TEM at an accelerating voltage of 200 kV. TEM images were analyzed by *Image J* software to estimate the size distribution of samples. The UV-Vis spectra of the samples was obtained using a Perkin Elmer-lambda 45 instrument in wavelength range of 200-800 nm. To compare the dispersion level and stability of aqueous solution of GO samples similar aliquots of each solution were taken every hour and the optical absorption of the diluted samples was recorded. Zeta potential of the prepared GO and siloxane/GO samples was measured by a Malvern instrument. The viscosity of aqueous solution of the prepared samples was compared using an Ubbelohde viscometer.

5. Fabrication of GO-based Thin Film Membranes

The membrane preparation procedure was started by immersing PES support in 2 g/L dopamine and 10 mM Tris buffer solution at pH 8.5 for 24 h. Dopamine was polymerized to form polydopamine on the PES support. GO-based thin film membranes were prepared by pressure-assisted self-assembly of aqueous solution of GO or siloxane/GO samples (100 mL) on a dopamine-treated PES support in a dead end cell. The thickness of GO-based thin films was changed by altering the concentration of GO and siloxane/GO solutions from 5 to 100 mg/L. To this end, different volumes (0.2 to 4 mL) of stock solution (2.5 mg/mL according GO weight) of the prepared GO and the siloxane/GO samples were placed into a 100 mL volumetric flask and diluted to the mark line to prepare 5, 10, 25, 50 and 100 mg/L solutions of each sample. The prepared membranes were named according to the type and the concentration of the solutions. For instance, thin film membranes prepared based on unmodified GO, GO-T1 and GO-T2 using similar concentration of 5 mg/L of the corresponding stock solution were named as GO/5, GO-T1/5 and GO-T2/5, respectively.

6. Physicochemical and morphological study of GO-based thin film membranes

SEM images were acquired on a Seron Technologies-AIS2100 system. The prepared GO-based thin film membranes were coated by a thin layer (~10 nm) of gold before tests by Quorum Technologies-Emitech system. Hydrophilicity of the prepared membranes was evaluated based on the measurement of water contact angles, using a Sony-SSC-DC318P video contact angle measurement system. At least six stabilized contact angles from different sites of each sample were obtained to calculate the average contact angle during 10 s. Membrane porosity (ε) was determined by gravimetric method [34]. Membrane porosity can be defined as Eq. (2):

$$\varepsilon = \frac{m_1 - m_2}{\rho_w \times A \times l} \quad (2)$$

where m_1 is the weight of the wet membrane; m_2 is the weight of the dry membrane; ρ_w is the water density (0.998 g/cm^3); A is the effective area of the membrane (m^2); l is the membrane thickness (m). To this end, the prepared membranes were fully dehydrated in an oven at 80 °C overnight and weighed. The dry membranes were then soaked in distilled deionized water at ambient conditions for 24 h and the wet weight of membranes was measured and the membrane porosity was estimated using Eq. (2).

The stability of the prepared membrane under physical stress was investigated using ultrasonic waves. The same sample sizes of the membranes were put in petri dishes and placed in an ultrasonic bath (100 W, 80 Hz), and a digital photo of membranes was taken in regular time intervals.

7. GO-based Thin Film Membrane Performance

Membrane performance was investigated by a laboratory-made dead-end filtration system with an effective membrane area of 9.6 cm^2. This system consisted of a feed tank pressurized with a nitrogen cylinder and a stirred cell used to evaluate water flux and solute rejection. Prior to each test, GO-based thin film membranes were immersed in DI water for 2 h. DI water was used to test the pure water flux of the membrane. For flux measurement the membrane was installed in the stirred cell and the flux was measured after stabilizing flux at transmembrane pressure of 2.5 bar. Water flux was calculated by weighing the permeated water at regular intervals. The membrane rejection was investigated using PG-

P and (MB) aqueous solutions (10 mg/L). The concentration of the feed and permeate solutions was measured by UV-Vis spectrophotometry. The pure water flux (J_w) was calculated using Eq. (3), where J is the water flux (L/m^{2}h), V_p is the permeate volume (L), A is the membrane area (m^2) and Δt is the filtration time (h) [35].

$$J_w = \frac{V_p}{A\Delta t} \tag{3}$$

The MB and PG-P rejection performance of all membranes was evaluated using feed concentration of 10 mg/L. For these experiments, the dead-end filtration cell was filled with 200 mL of the desired feed solution and pressurized. The rejection of the prepared membranes was calculated using Eq. (4) at a constant transmembrane pressure of 2.5 bar.

$$R\,(\%) = \left(1 - \frac{C_p}{C_f}\right) \times 100 \tag{4}$$

R is the rejection, C_p and C_f are the concentration of permeate and feed solution, respectively [35]. The permeate concentration of membranes was measured using UV-Vis spectroscopy technique. To make sure variations in separation performance of the prepared membranes were due to changes in the applied variable, all tests were repeated on four comparable membranes of each type.

Mean pore radius (r_m) was determined by filtration velocity method, which is a measure for the permeation and retention properties of membranes and is directly related to the filtration velocity and so structural parameters of the membrane. According to Guerout-Elford-Ferry equation, [34] r_m could be expressed as follows:

$$r_m = \sqrt{\frac{(2.9 - 1.75\varepsilon) \times 8\eta l Q}{\varepsilon \times A \times \Delta P}} \tag{5}$$

where η is water viscosity (8.9×10^{-4} Pa·s); l is the membrane thickness (m); ΔP is the operation pressure (bar) and Q is membrane flux. The calculated r_m of bare PES support was subtracted from the corresponding results obtained from GO-based thin film coated PES membranes to estimate the mean pore size of GO thin films.

The antifouling property of the prepared membranes was evaluated by calculating reversible fouling ratio (R_r), irreversible fouling ratio (R_{ir}) and flux recovery ratio (FRR). An aqueous solution of BSA with concentration of 500 mg/L and pH 7 (adjusted by phosphate buffer) was used as a model protein foulant for all fouling experiments [36,37]. Several resistances occur during fouling processes and total resistance ratio (R_t), which reflects total flux loss can be defined as Eq. (6):

$$R_t = \left(1 - \frac{J_p}{J_{w1}}\right) \times 100 \tag{6}$$

The prepared membrane was mounted in the dead-end cell and pure water flux (J_{w1}) was measured at transmembrane pressure of 2.5 bar for 90 min. Then, the permeation of membrane was studied using the aqueous solution of BSA at the same pressure to find the flux J_p. After flushing the membrane with DI water for 30 min, the pure water flux through the cleaned membrane was determined and named as J_{w2}. The total resistance is the sum of hydraulic resistance of the membrane, reversible fouling ratio, R_r, and irreversible fouling ratio, R_{ir}. R_r, which is also referred to as cake resistance, reflects the incidence of reversible phenomena such as concentration polarization and reversible depositions [38]. R_{ir} indicates the irreversible deposition onto the membrane surface or in the membrane matrix, such as adsorption and deposition of foulants on the membrane pore walls and surfaces [38]. R_r and R_{ir} can be calculated using Eqs. (7) and (8) [39].

$$R_r = \left(\frac{J_{w2} - J_p}{J_{w1}}\right) \times 100 \tag{7}$$

$$R_{ir} = \left(\frac{J_{w1} - J_{w2}}{J_{w1}}\right) \times 100 \tag{8}$$

The resistance of the membrane against fouling was evaluated in term of flux recovery ratio (FRR), expressed in Eq. (9).

$$FRR = \left(\frac{J_{w2}}{J_{w1}}\right) \times 100 \tag{9}$$

The stability of GO-based thin film membranes against chlorine attack was investigated using an aqueous solution of sodium hypochlorite (NaOCl, 500 mg/L). The prepared membranes were soaked in the NaOCl solution for 1 h and then rinsed thoroughly with DI water. The PG-P rejection of the membranes was measured before and after exposure to chlorine and the chlorine stability of membranes was evaluated from the extent of performance changes occurring after chlorine exposure [40].

RESULTS AND DISCUSSION

1. Physicochemical Characterization of the Synthesized Samples

FT-IR spectroscopy is an effective technique for analyzing functional groups of GO derivatives. Fig. 1 compares the FT-IR spectra of GO, GO-T1 and GO-T2 samples. GO sample showed bands at 1,063, 1,205, 1,381, 1,625, 1,727 and 3,428 cm^{-1} corresponding to alcoholic C-O stretching, etheric C-O stretching, O-H bending, C=C stretching, C=O stretching and O-H stretching vibration, respectively. As can be seen, the intensity of the above-mentioned bands was significantly attenuated in the FT-IR spectrum of the siloxane/GO samples and new bands appeared in these samples. Bands shown at 803, 1,024, 1,095 cm^{-1} were assigned to the vibrational bands of Si-O-Si, C-O-Si, and C-H, respectively, formed in

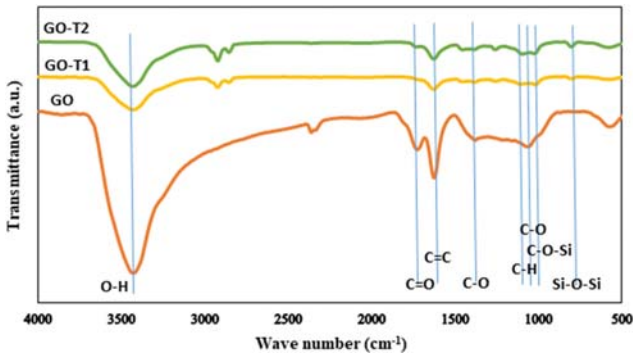

Fig. 1. FTIR spectra of GO, GO-T1 and GO-T2 samples.

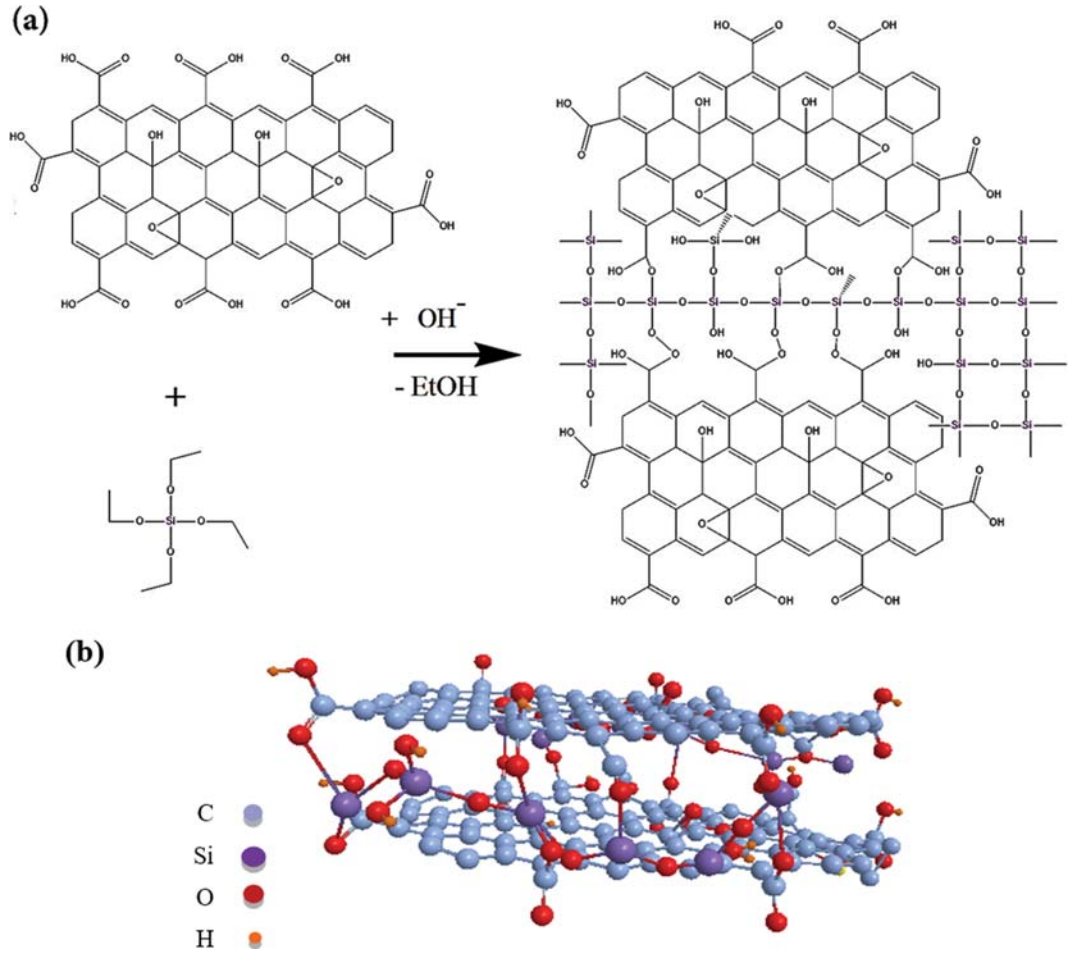

Fig. 2. (a) The reaction of GO and TEOS through sol-gel process and (b) schematic representation of GO nanosheets crosslinked by siloxane network.

the siloxane/GO samples [25].

To express the observed changes in numerical values the intensity of each band was divided by the intensity of the C=C stretching vibration of that sample and the obtained results are listed in Table S2. The C=C band was selected for normalization since it remained approximately unchanged in all samples. For GO, the band at 1,727 cm^{-1} corresponds to the C=O stretching vibration of carbonyl or carboxylic groups. The normalized intensity of C=O stretching vibration of carbonyl or carboxylic groups at 1,727 cm^{-1} varied from 0.57 in the GO sample to 0.26 and 0.30 for GO-T1 and GO-T2, respectively. This indicates that C=O groups have been eliminated or converted to other functional groups in the siloxane/GO samples. On the other hand, GO-T1 and GO-T2 showed additional bands at 803, 1,024, 1,095 cm^{-1} corresponding to Si-O-Si, C-O-Si, and C-H bonds, which confirmed the formation of siloxane network. The normalized intensity of Si-O-Si band in GO-T2 (0.27) sample was considerably higher than that obtained for GO-T1 (0.18), indicating a higher development level of siloxane network in the GO-T2 sample. Furthermore, a higher normalized intensity of C-H (1.11) and Si-O-C (0.72) was obtained for GO-T2 compared to those calculated for GO-T1, suggesting the formation of higher level of chemical bonds between GO and siloxane network in the GO-T2 samples.

FT-IR results confirmed the formation of siloxane network and their linkage to the carbonyl groups of GO, as shown in Fig. 2(a). A schematic representation of interactions between siloxane network and two GO nanosheets is also depicted in Fig. 2(b). The sol-gel process involves the hydrolysis reaction, which replaces –OET groups in TEOS with -OH groups, and subsequent condensation reactions in which the silanol groups produce siloxane bonds (Si-O-Si) and the by-products alcohol [41]. Hydrolysis, which occurs by the nucleophilic attack of OH^- anions on the Si atom through an SN2 mechanism (Fig. S1), is facilitated in the presence of alcohol as a homogenizing agent [41,42]. The rate and extent of this reaction is greatly affected by the strength and concentration of the catalyst (here, ammonium hydroxide) [41,42], while temperature and solvent are less effective [41]. The hydrolysis rate is also strongly pH-dependent and increases by over three orders of magnitude in aqueous solution between pH 3 and 8. The condensation reaction, which involves the nucleophilic attack of deprotonated silanol on a neutral silicate, continues until the maximum number of Si-O-Si bonds and the minimum number of terminal hydroxyl groups are achieved. This leads to the formation of three-dimensional particles which condense to the most

compact state leaving -OH groups on the outside [41]. The maximum condensation rate is achieved near neutral pH where significant concentration of both protonated and deprotonated silanol exist. Therefore, it can be deduced that the hydrolysis reaction occurred at a higher rate in the case of GO-T1, due to the addition of a higher amount of ammonium hydroxide at the beginning of the reaction. Similarly, the observed lower intensity of Si-O-Si band for GO-T1 can be attributed to the lower rate of condensation reaction at pH>7. In contrast, the condensation reaction was faster than the hydrolysis reaction in the case of GO-T2, confirmed by higher intensities of Si-O-Si and C-H bands.

The XRD patterns of GO, GO-T1 and GO-T2 samples are shown in Fig. 3. The characteristic peak of GO was observed in 11.49° corresponding to interlayer spacing of 7.7 A° (according to Bragg's law). This peak appeared at 10.7° and 9.95° for GO-T1 and GO-T2 samples, indicating an increase in the interlayer spacing of these samples to 8.28 A° and 8.85 A°, respectively. The broad char-

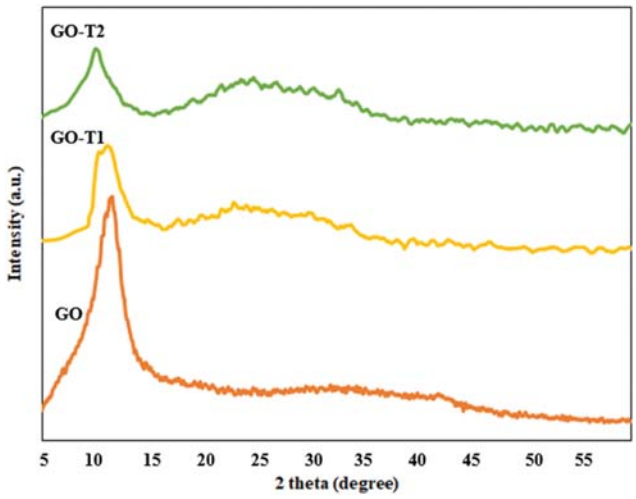

Fig. 3. XRD patterns of GO, GO-T1 and GO-T2 samples.

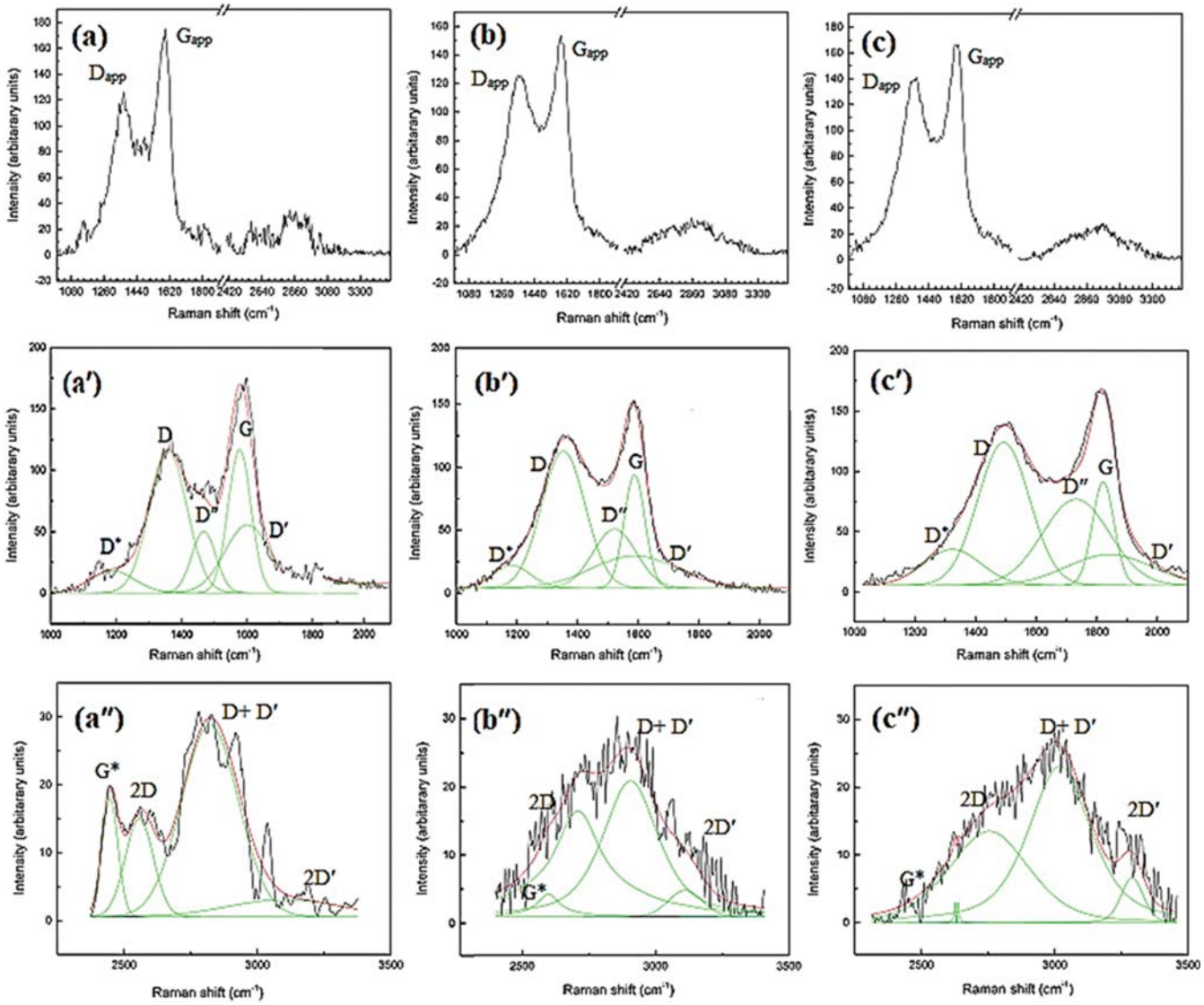

Fig. 4. Raman spectra of the prepared samples; (a) GO, (b) GO-T1 and (c) GO-T2. (′) First-order and (″) second-order Raman spectra of samples.

acteristic peak of SiO_2 in siloxane structure was observed at 23° in the XRD pattern of GO-T1 and GO-T2 samples [43]. Using Scherrer equation, the mean height of GO stacks was estimated to be about 25.9, 39.8 and 46.4 A° for GO, GO-T1 and GO-T2 samples, respectively. By dividing the stack height to the calculated value of the interlayer spacing of the corresponding samples, the number of stacked layers in each sample was determined, which was higher for the siloxane/GO samples, GO-T1 (~4.8) and GO-T2 (~5.24), compared to the unmodified GO sample (3.36). The higher number of stacked layers and the larger interlayer spacing of siloxane/GO samples indicate the successful intercalation of siloxane networks between GO nanosheets through the sol-gel process. Moreover, GO-T2 appeared to have a larger interlayer spacing compared to GO-T1. This was attributed to the higher rate of condensation reaction and the formation of larger siloxane networks between GO nanosheets, as will be discussed later using TEM images.

Raman spectroscopy is a non-destructive technique commonly used to characterize both electronic and structural properties of graphene-based materials. The Raman spectrum of GO consists of two prominent characteristic peaks: G band originating from the E2g phonon, the D band corresponding to the A1g breathing mode of k-point phonons of A1g symmetry. G band belongs to sp^2 carbon atoms and D band is assigned to local defects observed due to disorders mostly at the edges of GO nanosheets [44]. The position, relative shapes and intensity of these peaks provide valuable information about the structural and electronic characteristics of graphene-based materials [44]. Fig. 4(a)-(c) shows the Raman spectra of GO, GO-T1 and GO-T2. For the GO sample (Fig. 4(a)), D and G bands appeared at 1,360 cm^{-1} and 1,577 cm^{-1}, respectively. These bands were also observed in the Raman spectra of GO-T1 and GO-T2 samples, while their intensity changed compared to those observed in the GO sample. D and G peaks have been named as apparent D (D_{app}) and G (G_{app}) peaks in Fig. 4(a) to (c). First-order part of the spectra was deconvoluted to five bands by Gaussian function corresponding to D, G and D′ bands and two poorly understood peaks, named as D* and D″, as shown in Fig. 4((a′) to (c′)).

The band parameters obtained from the fit process are presented in Table S3. The mathematical relation of these bands can provide valuable information about crystallinity, structural defects and oxidation or reduction degree of samples [45]. The intensity ratio of D″ and G peaks (ID″/IG) is often used for evaluating the level of crystallinity of samples: higher value reveals lower crystallinity [46]. Generally, the ID″/IG ratio (Table S3) appeared to be higher for the siloxane/GO samples compared to the unmodified GO, indicating higher level of disorder in the siloxane incorporated GO samples. The highest ID″/IG ratio was obtained for the GO-T2 sample, which was prepared using a lower concentration of ammonium hydroxide at a higher temperature. This indicates an increase in the sp^3 amorphous carbon phase in GO-T2 due to higher rate of condensation reaction and consequently higher development of siloxane networks. The position of the D″ and D* peaks was also shifted to higher wavenumber values moving from GO (Fig. 4(a′)) to GO-T2 (Fig. 4(c′)) sample. The position of these bands was considered as an indication to estimate the reduction degree of GO through the sol-gel process. It has been shown that the D″ band is related to amorphous phases since its intensity decreases with the increase of the crystallinity [47]. As can be seen, the D″ band intensity increased in the siloxane/GO samples and the highest intensity was achieved for the GO-T2 sample (see Fig. 4((a′) to (c′))), indicating the higher amorphous nature of this sample. Furthermore, the highest intensity of D* band was obtained for the GO-T2 sample, shown in Fig. 4(c′), implying the presence of a higher percentage of sp^3 carbon in this sample [48]. This is in good agreement with the higher intensity of C-H band observed in the FT-IR spectrum of GO-T2 sample, shown in Fig. 1, which was explained by the lower rate of hydrolysis reaction and the higher rate of condensation reaction at pH near 7, applied for the synthesis of this sample. The second-order Raman spectrum of the prepared sample was deconvoluted by Gaussian to G*, 2D, D+D′ and 2D′ bands as shown in Fig. 4(a″) to (c″). For all the prepared samples, the 2D band appeared as a broad single peak, indicating that different planes possess randomly oriented structure with a stacking order comparable to graphite [49]. The position of the 2D and D+D′ bands can be used to estimate the percentages of sp^2 carbon in GOs. A decrease in the broadness and intensity of the 2D band occurred moving from the GO sample (Fig. 4(a″)) to the siloxane/GO samples (Fig. 4-parts (b″) and (c″)). This indicates a decrease in the lifetime of photo-excited electron-hole pairs [50], due to an improvement in the electron-electron interactions in the siloxane/GO samples, especially in the case of GO-T2. The subtraction of inferred D′ mode (D'_{inf}) and G_{app} ($D'_{inf}-G_{app}$) was applied to determine the C/O ratio [45]. D'_{inf} was obtained by dividing the energy of the 2D′ mode by 2 [45]. Negative values of $D'_{inf}-G_{app}$ represent GO-like structures and the positive values ($0<D'_{inf}-G_{app}<25$) reflect rGO-like structures. In general, C/O ratio is less than 10 for GOs while for rGOs, C/O ratio is between 10 and 500 [45]. For all samples, a negative value of $D'_{inf}-G_{app}$ was obtained (Table S3) and as it was expected the GO sample (−55.0) appeared to have the highest value. $D'_{inf}-G_{app}$ shifted to lower negative values for GO-T1 (−30.5) and GO-T2 (−3.5), implying a decrease in the oxidation level of the siloxane/GO samples. This was attributed to the formation of chemical bonds between siloxane networks and GO nanosheets, as confirmed by the presence of Si-O-C bands in the FT-IR spectrum of siloxane/GO samples (Fig. 1). According to equations described elsewhere [45], the C/O ratio of GO-T1 and GO-T2 samples was estimated to be about 10. This confirms, despite the fact that the oxidation level of the siloxane/GO samples was lower compared to the GO sample, they still possess GO nature.

TEM images of GO-T1 and GO-T2 samples are shown in Fig. 5((a), (a′)) and ((b), (b′)), respectively. The overlap of GO sheets results in formation of darker areas in TEM images of the siloxane/GO samples. The GO sheets exhibit wrinkled morphology, suggesting that the as-prepared siloxane/GO are few layers thick. The formation of siloxane network on GO sheets can be observed as dark spots in the TEM images of samples. The uniform distribution of small dark spots in the TEM images of GO-T1 (shown in Fig. 5((a), (a′))) reveals the formation of relatively uniform siloxane network wrapped up on GO sheets. However, the presence of randomly distributed larger dark spots in the TEM images of GO-T2 (Fig. 5(b) and (b′)) shows that larger agglomerates have been formed in this sample, while they are still attached to the GO sheets.

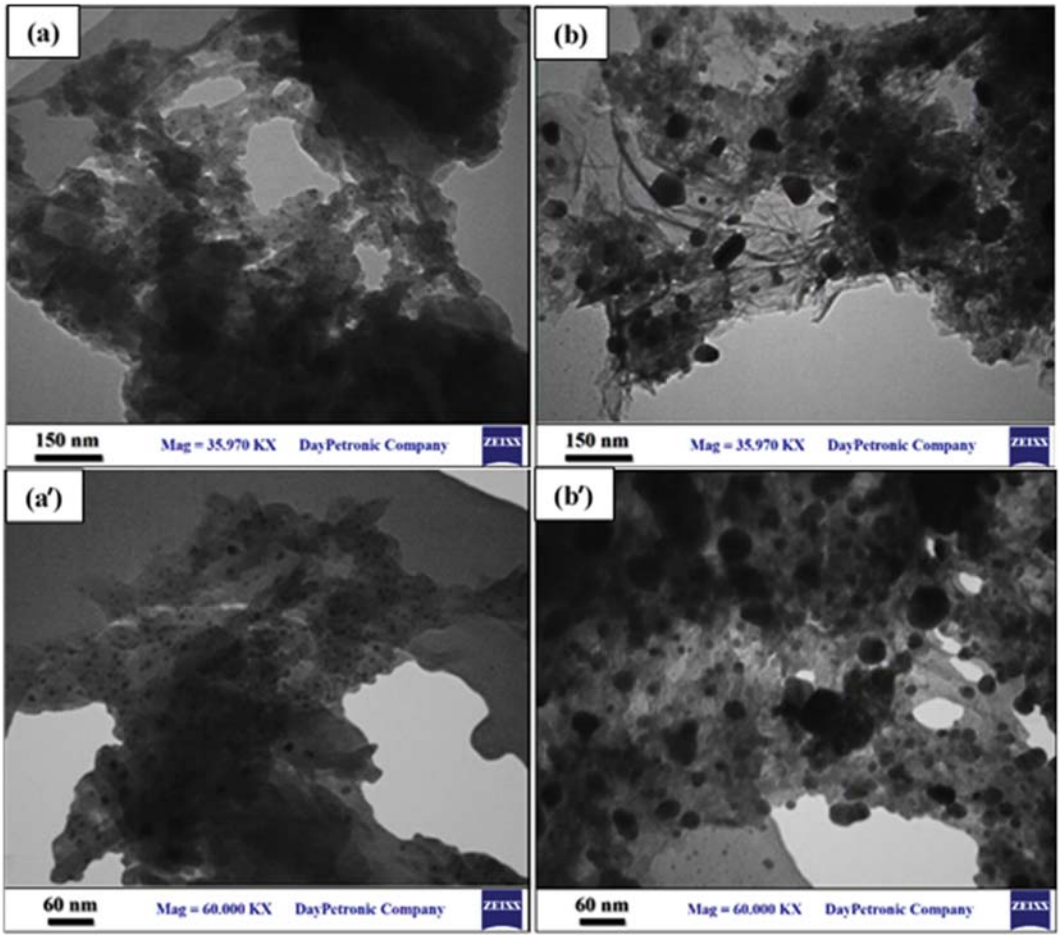

Fig. 5. TEM images of the synthesized siloxane/GO samples: ((a), (a′)) GO-T1 and ((b), (b′)) GO-T2 at two magnifications.

As mentioned, condensation reactions lead to the formation of three-dimensional particles which are condensed to the most compact form leaving -OH groups on the outside, which serve as nuclei [41]. Further growth of particles occurs through Ostwald ripening mechanism as highly soluble small particles dissolve and re-precipitate on larger, less soluble nuclei. Particle growth stops when the solubility difference of the smallest and largest particles becomes only a few mg/L. Therefore, particle growth continues to form larger sizes at higher temperatures, due to greater solubility [41]. It has been established that above pH 7 particle growth occurs mainly by the addition of monomers to more highly condensed particles rather than by particle aggregation since the silica particles are appreciably ionized and mutually repulsive. Considering the above-mentioned facts, the smaller size of siloxane networks formed on GO nanosheets in GO-T1 sample can be attributed to the higher dissolution of silica at pH above 7 and that the particle growth occurred mainly by the addition of monomers to more highly condensed particles rather than by particle aggregation, which is the case for the GO-T2 sample prepared using a lower concentration of ammonium hydroxide at higher temperature.

The size distribution histogram of siloxane network in GO-T1 and GO-T2 samples is presented in Fig. S2. As can be seen, a dominating fraction of very small siloxane network (4-5 nm) was formed in GO-T1, while in the case of GO-T2 aggregation of siloxane network occurred and the particle size distribution increased significantly. The dominating particle size of siloxane network (5-15 nm) in GO-T2 was about five-times higher. Considering the ultrasonic process used during the sample preparation for TEM, these results clearly demonstrate that the siloxane network has been successfully anchored on GO nanosheets.

UV-Vis spectroscopy was used to investigate the dispersion level of the prepared GO samples in water. For these experiments, equal amount of each sample was separately dissolved in de-ionized water (2.5 mg/mL), diluted by a factor of 100 and homogeneously dispersed using an ultrasonic bath (37 KHz, 70 W) at room temperature. The stability of GO solutions was studied by sampling and recording the UV-Vis spectra of the obtained homogeneous GO solutions over a month while solutions were undisturbed. The absorption intensity of the unmodified GO sample (Fig. S3(a)) decreased rapidly after 4 h, while the absorption intensity remained constant for GO-T1 and GO-T2 (shown in Fig. S3-parts (b) and (c)) even after a month. GO nanosheets, which contain hydrophilic oxygenated groups on their basal planes and edges, start to sediment after a short time due to sedimental collision process and gravity forces. Furthermore, larger interlayer spacing improves the chance of water entrance between GO nanosheets and so contributes to the increment of hydration. The stability analysis of the prepared GO solutions clearly demonstrated that the formation of hydro-

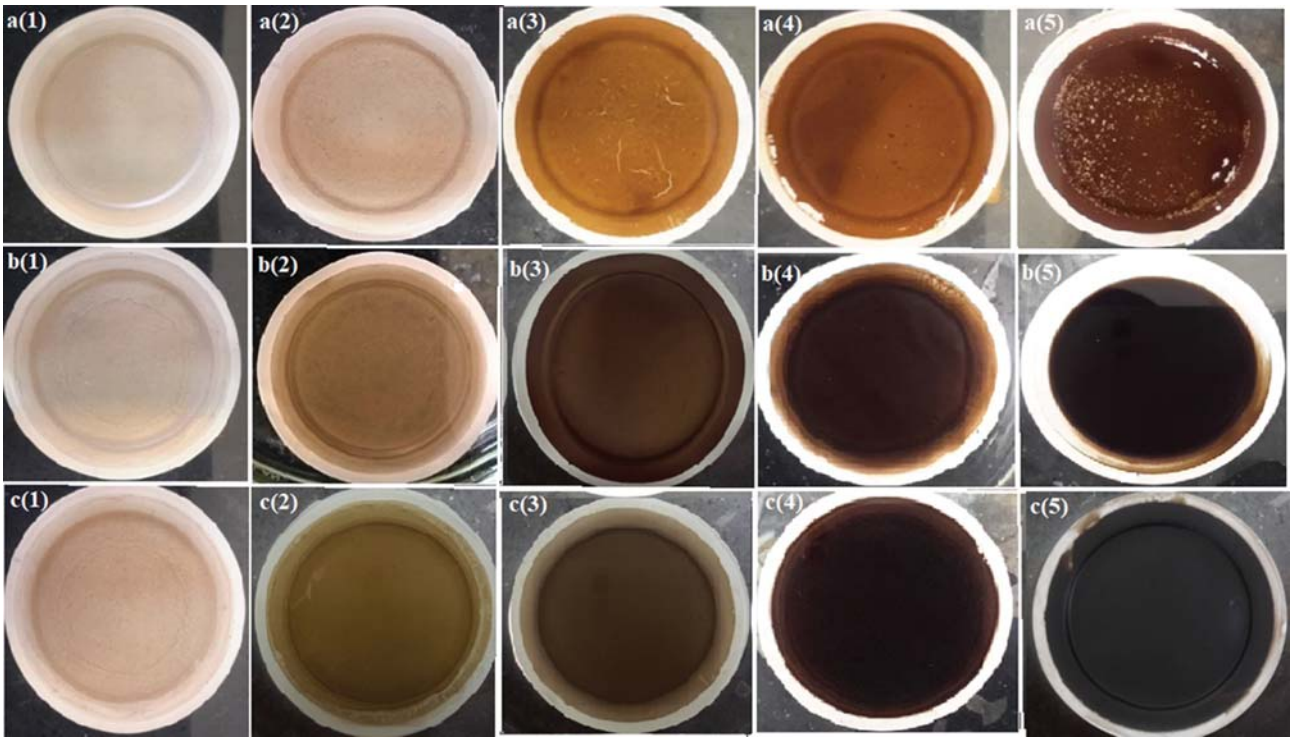

Fig. 6. Digital images of PES-supported GO thin film membranes prepared by pressure-assisted self-assembly of aqueous solution of (a(1)-a(5)) GO, (b(1)-b(5)) GO-T1 and (c(1)-c(5)) GO-T2, by increasing concentration with sequence of 5, 10, 25, 50 and 100 mg/L (left to right).

philic siloxane networks between GO nanosheets has improved the hydration level of the siloxane/GO samples due to their larger interlayer spacing, confirmed by XRD results presented in Fig. 3.

Zeta potential measurement was applied to further evaluate the dispersion behavior of the prepared GO samples. The absolute zeta potential values of GO-T1 and GO-T2 were estimated to be about 32.0 mV and 30 mV, respectively. However, for GO, the absolute zeta potential (26.2 mV) was less than 30 mV, confirming the lesser dispersion stability of the GO sample. As can be seen, GO-T1 appeared to have a higher zeta potential and surface charge compared to GO-T2. This can be explained by the higher rate of hydrolysis reaction and the lower rate of condensation reaction in this sample. As discussed earlier, above pH 7 all the condensed species are more likely to be ionized, and due to repulsive forces particle growth takes place via adding monomers to more highly condensed particles possessing -OH groups on the outside, which serve as nuclei, rather than by particle aggregation. This results in the formation of smaller particles with higher negative charge density in GO-T1 sample [41,42]. Thus, the lower zeta potential of GO-T2 can be attributed to the higher condensation rate and the formation of larger particles as a result of particle aggregation, possessing lower charge densities. The relative viscosity of aqueous solutions of GO-T2 and GO-T1 was also estimated to be about 1.27 and 1.37, respectively. The higher viscosity of GO-T2 solution was attributed to the incorporation of higher level of siloxane networks between GO nanosheets.

2. GO Membrane Performance

The thickness of PES-supported GO-based thin film membranes was changed by altering the concentration of aqueous solution of GO and siloxane/GO from 5 to 100 mg/L. Digital images of the prepared membranes are presented in Fig. 6. By increasing the concentration of the applied solution, the thickness of thin film membranes increased and so their color changed from light brown to dark brown. All GO-T1 and GO-T2 membranes appeared to have uniform surfaces and no obvious defects such as pores or cracks were observed in these samples even at the highest concentration as shown in Figs. 6(b(5)) and 6(c(5)) for GO-T1/100 and GO-T2/100, respectively. However, for GO membranes, increasing the GO concentration to values higher than 50 mg/L resulted in the formation of defects on the obtained GO/100 membrane (Fig. 6(a(5))), which is not favorable for their application in membrane separation processes. The separation performance of the prepared membranes was evaluated by two target species: MB as cationic organic dye and PG-P as neutral organic molecule. The removal of bare PES and polydopamine coated PES support was negligible either for MB or PG-P.

Generally, the ability of GO-T1- and GO-T2-based membranes to reject MB (Fig. 7(a) and PG-P (Fig. 7(b)) was improved by increasing the concentration of GO-T1 and GO-T2 solutions (consequently the thickness of thin film membranes) and reached maximum values using solution concentration of 50 mg/L. However, the application of higher concentration (>50 mg/L) resulted in no significant changes in the separation performance of these membranes. Similar trend was also observed for GO membranes, while the rejection decreased at concentration higher than 50 mg/L due to formation of pores and cracks, as shown in Fig. 6. GO-T2 based

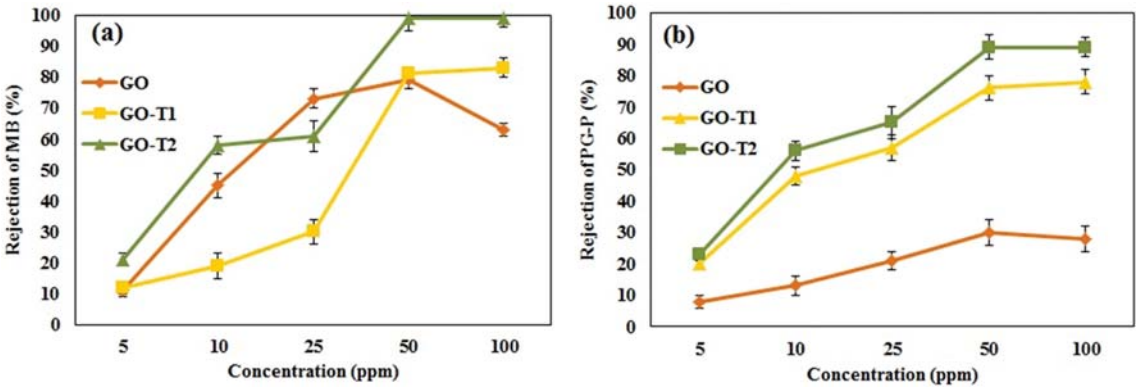

Fig. 7. Rejection of the prepared PES-supported GO thin film membranes for (a) MB and (b) PG-P.

membranes showed higher ability to remove cationic species of MB (Fig. 7(a)) and neutral species of PG-P (Fig. 7(b)) compared to GO-T1 based membranes at all concentrations. This was attributed to further development of siloxane network in the GO-T2 samples, as discussed earlier.

Comparing the separation performance of GO membranes in Fig. 7 reveals these membranes act better to remove positively charged MB rather than neutral species of PG-P. The highest PG-P rejection achieved using GO/50 membrane was 30%, which was about 50% lower than that achieved for MB rejection. The ability of GO-T1- and GO-T2 membranes to reject MB and PG-P was generally better than for GO membranes, especially in case of PG-P. The maximum MB removal of 99% was obtained by GO-T2/50 membranes, which was about 27% and 13% higher than that achieved by GO/50 and GO-T1/50 membranes, respectively. Similarly, GO-T2/50 membranes could remove 88% of PG-P, while the maximum PG-P removal obtained by GO/50 membranes was about three-times lower. Although GO-T1 based membranes showed considerably higher ability, compared to GO membranes, to remove PG-P (Fig. 7(b)), however, their separation performance was considerably weaker than that observed for GO-T2 based membranes at all concentrations. The higher ability of GO-T2 based membranes to reject MB cannot be explained only by the stronger electrostatic forces between positively charged MB and negatively charged siloxane/GO, since GO-T2 showed a lower zeta potential compared to GO-T1. Considering that the molecular weight of PG-P (570.7 g/mol) is higher than that of MB (319.85 g/mol), the obtained results revealed that the separation performance of GO membranes is more affected by the charge of species not the size of molecular species. In contrast, for GO-T1 and GO-T2 mem-

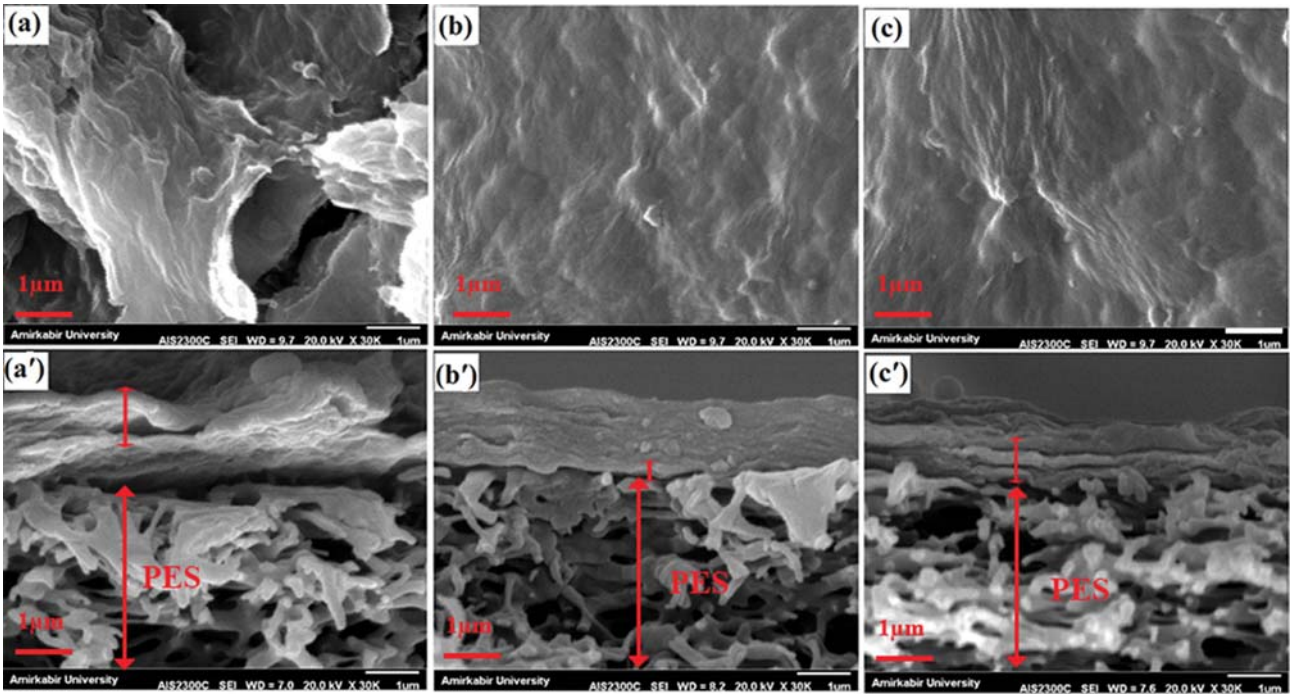

Fig. 8. The longitudinal and cross-sectional (indicated with (′)) SEM images of the prepared PES-supported GO thin film membranes; (a) GO-, (b) GO-T1- and (c) GO-T2-based membranes.

branes it seems size exclusion based separation process plays the main role.

To evaluate the contribution of adsorption and size exclusion processes in the removal percentage of MB and PG-P by the prepared thin film membranes, equal amount of the dried powder of GO, GO-T1 and GO-T2 samples was separately dispersed in 100 mL of MB and PG-P solutions which had the same concentration of 10 mg/L. The concentration of the prepared solutions was measured every 20 min in a time span of 3 h, using a UV-Vis spectrophotometer. Although the separation ability of the prepared thin film membranes was evaluated over an hour, however, to ensure that the maximum adsorption was achieved by powder samples, the adsorption process was extended for 3 h. The variations in removal percentage of MB and PG-P as a function of time are shown in Fig. S4. As can be seen, the highest adsorption occurred during the first 20 minutes and afterward no obvious change was detected. As expected, all samples absorbed MB by a higher extent compared to PG-P (see Table S4). However, in contrast to the results obtained from studying the separation performance of the prepared membranes (Fig. 8(a)), the highest MB removal was achieved by the GO-T1 sample. This is in good agreement with data obtained from zeta potential measurements, which showed the GO-T1 sample has the highest negative surface charge, and consequently can adsorb a higher amount of positively charged MB in aqueous solution due to stronger attraction electrostatic forces. In case of neutral species of PG-P, the adsorption follows ion-induced dipole interactions [51], which are weaker compared to electrostatic forces. The higher adsorption of PG-P by the GO-T1 sample (shown in Table S4) can therefore be explained by its higher zeta potential and surface charge, compared to GO-T2, providing larger ion-induced dipole interactions. In addition to the adsorption process, the size exclusion process contributes to the separation performance of the siloxane/GO membranes and is assumed to play the major role in the PG-P removal since it is a neutral species. Results presented in Table S4 suggest that the adsorption process makes a small contribution (~9%) in the separation performance of the GO-T2 membranes and that the presence of larger siloxane networks in these membranes restricts the penetration of PG-P in a higher level compared to GO-T1 membrane.

3. Physicochemical and Morphological Characterization of Membranes

GO/50, GO-T1/50 and GO-T2/50 were selected as thin film membranes with the best separation performance in each series and further analysis was performed on these samples. Fig. 8 displays the longitudinal and cross-sectional SEM images of the prepared thin film membranes. As can be seen, aggregation of GO nanosheets occurred in the GO/50 membrane due to higher precipitation rate of unmodified GO compared to siloxane/GO, leading to formation of micro-size voids and gaps at the top layer. This explains the lower ability of the GO membrane to reject cationic and neutral species. On the contrary, GO-T1/50 (Fig. 8(b)) and GO-T2/50 (Fig. 8(c)) membranes appeared to have denser and uniform surface morphologies compared to GO/50. The anisotropic layer-structure of the prepared thin film membranes can be observed in the cross-sectional SEM images shown in Fig. 8((a')-(c')). Comparing these images revealed that the deposited unmodified GO membrane (Fig. 8(a) possessed a higher thickness (~2 μm) and was detached from the PES membrane at some regions. The adhesion of GO nanosheets to the PES support was improved by incorporating siloxane network and uniform thin films were formed in GO-T1/50 (Fig. 8(b')) and GO-T2/50 (Fig. 8(c')). The higher thickness of GO-based layer in the GO-T2/50 membrane was attributed to further development of siloxane network in the GO-T2 sample compared to the GO-T1/50. The formation of lamellar structure at GO-T2/50 membrane affirms this issue. Results demonstrate that the higher stability of the siloxane/GO solutions reduces the rate of deposition and provides the required time for the rearrangement of GO nanosheets to form smoother and defect-free thin films.

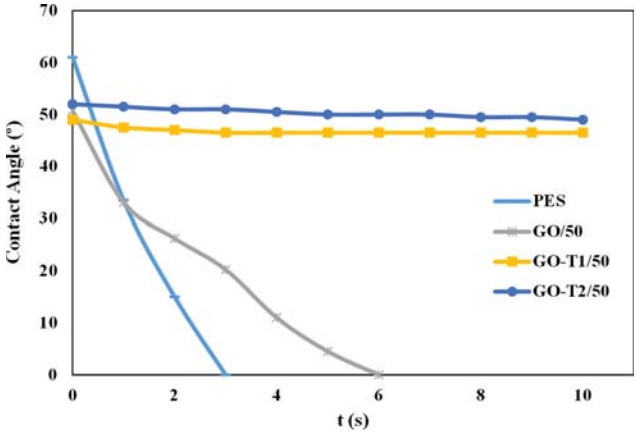

Fig. 9. Variation in water contact angle over time range of 0-10 s for the prepared membranes.

Fig. 9 exhibits the variation in water contact angle as a function of time for the prepared membranes. Generally, there is an inverse relationship between water contact angle and hydrophilicity - smaller contact angle, higher surface hydrophilicity. The wettability level of a membrane surface is determined by its chemical composition and morphology. For hydrophilic membranes, the surface hydrophilicity also increases by increasing the surface roughness [52]. The initial water contact angle was calculated to be about 61°, 51°, 49° and 51° for pristine PES, GO/50, GO-T1/50 and GO-T2/50 membranes, respectively. The highest initial contact angle was obtained for PES membrane, but the water drop vanished after 3 s due to the presence of larger pores at the surface of this membrane. The initial contact angle for GO/50 appeared to be about 51°, implying a higher hydrophilic nature of this membrane compared to PES, owing to the presence of hydrophilic oxygen-containing functional groups on GO nanosheets and the uneven surface morphology of this membrane (Fig. 8(a)). However, the water drop disappeared after 6 s from the top surface of GO/50 due to the formation of micrometer-scale gaps in this membrane (see Fig. 8(a)). The contact angle on GO-T2/50 was the same as that obtained for GO/50 and remained constant over the applied time range (10 s). This was attributed to the denser and smoother surface morphology of GO-T2/50 membrane. A lower contact angle (49°) was observed for GO-T1/50 compared to GO-T2/50. As discussed earlier, the size and surface charge of siloxane networks can be greatly

affected by altering the sol-gel synthesis parameters. This resulted in obvious differences in the longitudinal and cross-sectional morphology of the siloxane/GO thin film membranes. GO-T2/50 showed a denser and more ordered lamellar structure, leading to a slightly lower surface wettability of this membrane compared to GO-T1/50. Different surface wettability of membranes can also be explained considering the surface charge of siloxane networks formed between GO nanosheets. Therefore, the lower water contact angle and so the higher hydrophilicity of GO-T1/50 membrane can be attributed to the presence of smaller siloxane networks having higher surface charges, as confirmed by Zeta potential measurements.

The pure water flux of the fabricated membranes was measured at transmembrane pressure of 2.5 bar after 90 min of compaction with DI water. The GO/50, GO-T1/50 and GO-T2/50 membranes showed pure water flux of 623.7, 91.7 and 78.1 $L{\cdot}m^{-2}h^{-1}$, respectively (Table 1). GO/50 membrane possessing the most uneven and porous top surface structure showed the highest pure water flux. The water contact angle measurements showed that GO/50 and GO-T2/50 have comparable surface hydrophilicity but the presence of siloxane network between GO nanosheets restricted free movement of water in the siloxane/GO samples. The pure water flux of GO-T1/50 membranes with the lowest water contact angle (highest hydrophilicity) was about 18% higher than that of GO-T2/50 membranes. Results show that the formation of siloxane network between GO nanosheets affects the morphology more severely than the hydrophilicity of GO thin film membranes due to formation of denser and smoother surface in the siloxane/GO samples, especially in the case of GO-T2/50. Fig. 10 depicts the water permeation mechanism of the PES-supported siloxane/GO thin film membrane.

Table 1. The porosity and pore size of the prepared membranes

Sample name	Water contact angle (°)	Pure water flux ($L{\cdot}m^{-2}h^{-1}$)	ε	r_m (nm)
GO/50	51	623.7 (±10.0)	0.85	28.0
GO-T1/50	49	91.7 (±6.0)	0.72	5.5
GO-T2/50	51	78.1 (±5.0)	0.40	8.5

Results obtained from pure water flux measurements are in good agreement with the calculated porosity and pore size of the membranes listed in Table 1. As can be seen, adding siloxane network generally led to a decrease in the total porosity (ε) and the mean pore radius (r_m) of GO-T1/50 and GO-T2/50 compared to GO/50. While the total porosity of the membranes changed in range of 0.85 to 0.4, moving from GO/50 to GO-T2/50, the corresponding mean pore size of membranes varied in a significantly larger range (28.0 nm to 5.5 nm). Although, mean pore size of the GO-T1 membrane (5.5 nm) was smaller, the GO-T2 membrane showed higher MB and PG-P rejection. This was attributed to the development of larger siloxane network in the GO-T2 sample and also formation of thicker selective layer on the PES support.

The mechanical stability of the prepared membranes was investigated by ultrasonication test. Digital photographs of the prepared membranes before and after ultrasonication are shown in Fig. S5.

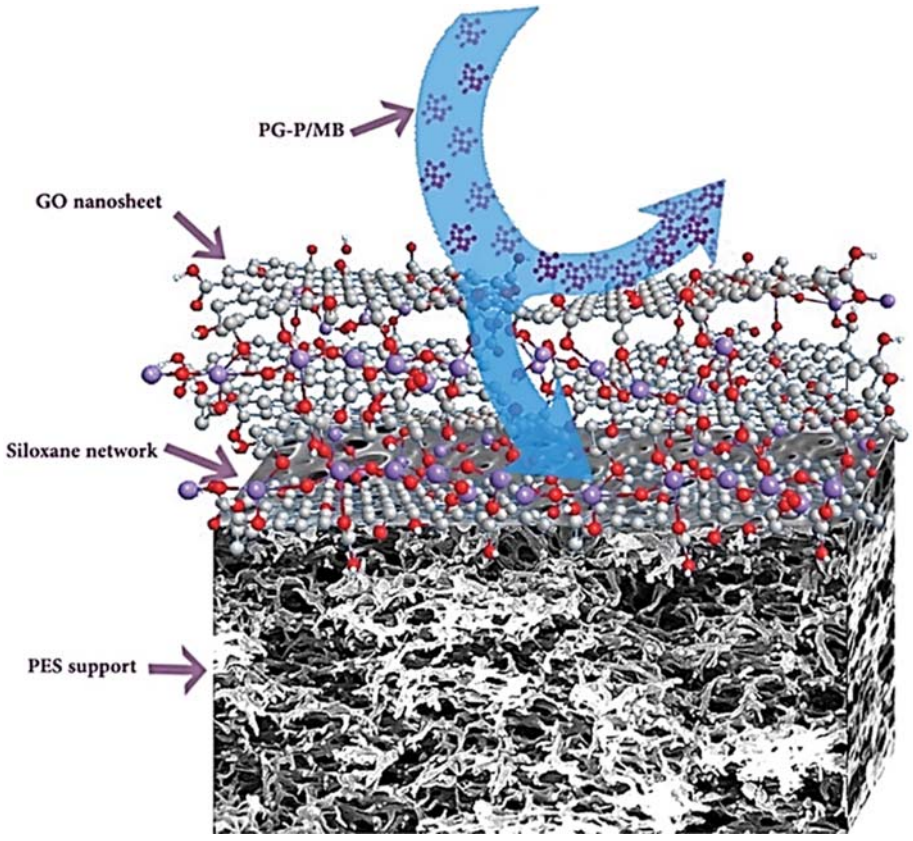

Fig. 10. The mechanism of water permeates and PG-P or MB rejection in the siloxane/GO membrane.

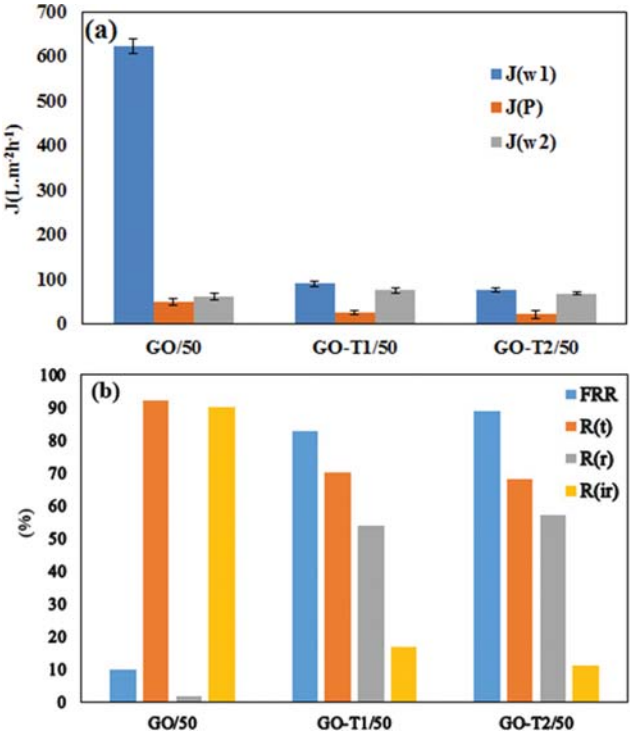

Fig. 11. Fouling behavior of PES-suppoted GO-based thin film membranes; comparing (a) initial pure water flux (J_{W1}), BSA permeate flux (J_P) and the second pure water flux (J_{W2}) and (b) FRR, R_t, R_r and R_{ir} of the fabricated membranes.

As can be seen, the GO/50 thin film membrane was destroyed in five seconds (Fig. S5(a′)) and completely delaminated after 1 min (Fig. S5(a″)), while the GO-T1/50 (Fig. S5-parts (b′) and (b″) and the GO-T2/50 (Fig. S5-parts (c′) and (c″)) membranes were quite stable during 1 h test time. After 1 h, the PES support membrane started to be destroyed. Results confirmed that the siloxane/GO membranes have higher mechanical stability compared to the GO membrane, implying the positive impact of the siloxane network on the mechanical stability of the GO nanosheets.

Fig. 11(a) compares J_{W1}, J_P and J_{W2} of membranes. It has been shown that foulants accumulate at a higher level on membranes with greater surface irregularity. As can be seen, J_{W1} value decreased with the incorporation of siloxane network between GO nanosheets. The BSA permeate flux of the membranes, J_P, was considerably lower than their corresponding pure water flux, due to the deposition of BSA foulants on the membrane surface. GO-T1/50 and GO-T2/50 membranes appeared to have similar permeate flux, which was lower than that observed for GO/50 membrane. This can be explained by smoother and denser surface morphology of the siloxane/GO thin films compared to GO/50 membranes. The second pure water flux of membranes (J_{W2}), which was acquired after BSA permeation analysis, decreased significantly (~90%) in the case of GO/50 membrane due to its rougher and irregular surface morphology. For this membrane, J_{W2} (62.7 $L \cdot m^{-2} \cdot h^{-1}$) was even lower than that achieved for GO-T1/50 (76.3 $L \cdot m^{-2} \cdot h^{-1}$) and GO-T2/50 (69.4 $L \cdot m^{-2} \cdot h^{-1}$). The water flux drop for membranes incorporated with siloxane network was considerably lower: 17% and 11% for GO-T1-50 and GO-T2/50 membranes, respectively. It has been shown that the morphological and physicochemical properties of membrane surface strongly affect the fouling behavior of membranes [53]. The presence of siloxane network in GO-T1/50 and GO-T2/50 membranes, which resulted in formation of smoother and denser surface structure improved both the rejection and the antifouling abilities of the siloxane/GO membranes. The extent of flux recovery of the membranes after fouling with BSA was followed by calculating FRR. As Fig. 11(b) shows, the GO-T2/50 membrane exhibited the highest FRR value (89%), implying a higher flux recover capacity and antifouling ability of this membrane. The FRR value for the GO/50 membrane (~10%) was about nine-times lower than that achieved for the GO-T2/50 membrane. Foulants are expected to be adsorbed in the valleys of rough membranes, resulting in clogging of the valleys and reducing the membrane flux [54]. Considering that the antifouling evaluation of membranes was carried out at pH above the isoelectric point of BSA (4.5-5), BSA is assumed to be ionized and negatively charged. Therefore, it was expected that GO-T1/50 having a higher negative surface charge exhibits better antifouling due to the stronger repulsive forces. However, in practice, GO-T2/50 has a more ordered lamellar structure with a slightly lower surface wettability provided the best antifouling properties. Results show that antifouling characteristic of GO membranes is more affected by membrane surface morphology rather than its surface charge [55].

For evaluation of fouling features of the membranes, the total fouling resistance, R_t, reversible fouling ratio, R_r, and irreversible fouling ratio, R_{ir}, are compared in Fig. 11(b). As expected, the GO/50 membrane has the highest R_t and R_{ir} values. However, the GO-T2/50 membrane shows the lowest R_t (68%) and R_{ir} (11%), and the highest R_r (57%). R_{ir}, which is also named as pore fouling, is caused by adsorption, precipitation or trapping of the foulant on the membrane surface or pores. GO membrane due to its rougher surface is exposed to the highest irreversible fouling, which is hardly removed during flushing of the membrane with water. The R_t value for GO-T1 and GO-T2 membranes is comparable; however, further development of siloxane network in the GO-T2/50 membrane led to an increase (~3%) in the R_r value and a decrease (~6%) in the R_{ir} value of this membrane compared to the GO-T1/50 membrane.

The chlorine resistance performance of the prepared membranes was studied by evaluating their physical stability and rejection properties before and after 1 h exposure to aqueous NaOCl solutions. The delamination and degradation of GO thin film membrane occurred in the GO/50 membrane after 30 min exposure to chlorine, so no membrane separation tests could be carried out on this membrane. However, for the GO-T1/50 and GO-T2/50 membranes no sign of degradation was observed even after 1 h exposure to chlorine. The separation performance of these membranes was evaluated after exposure to NaOCl by filtration of an aqueous solution of PG-P (10 mg/L) through the membranes in a dead-end system. The membranes appeared to retain about 95% of their rejection ability even after 1 h exposure to chlorine solution, indicating the higher chemical stability of the siloxane/GO thin film membranes. The prepared siloxane/GOs appeared to have higher interlayer spacing, higher zeta potential and so higher dis-

Table 2. Comparison of the rejection and pure water flux of GO-based nanofiltration membranes

Membrane name	Membrane type	The removed species	Rejection (%)	Pure water flux ($L \cdot m^{-2} \cdot h^{-1}$)	Reference
GO/TiO_2	Free standing	MO*	55	7	[17]
rGO/SiO_2	Packed bed	MB	-	-	[26]
GO/SiO_2	PES-supported	Glucose	85	90	[28]
GO/TiO_2	PSF-supported	MB	70	45	[57]
GO/borate	PAN**-supported	MB	88	50-100	[58]
GO/TMC	PSF-supported	MB	46	272	[11]
GO/Boron Nitride	PES-supported	MB	99-100	4	[59]
GO-T2/50	PES-supported	MB	99	78	Present work
GO-T2/50	PES-supported	PGP	88	78	Present work

*Methyl Orange
**Polyacrylonitrile

persion stability in aqueous media compared to the unmodified GO sample. This gave rise to slow and more uniform sedimentation of the siloxane/GOs during filtration process and consequently production of thin film membranes having denser and smoother morphology. The slower sedimentation rate of the siloxane/GO samples also provided the required time for rearrangement of GO nanosheets to find preferred interactions with each other and the PES membrane. This resulted in the formation of thinner, highly ordered and relatively defect-free siloxane/GO thin films which had higher adhesion to the PES support compared to the unmodified GO thin films. These interesting features also contributed to the higher mechanical and chemical stability of the siloxane/GO membranes, which are prerequisites for their applications in separation processes.

The comparison of the separation performance of the prepared membranes in this work with previously reported nanofiltration membranes can be followed in Table 2 [11,17,26,28,56-59]. A few works have been reported describing the preparation and the application of PES-supported GO/SiO_2- or GO/TiO_2-based membranes for the desalination or waste water treatment purposes [17, 26-28]. Some of these membranes have been prepared via a two-step method; depositing GO thin film membrane on a porous polymeric substrate as the support, and then modifying the thin film membrane with the desired hydrophilic nanostructures [28]. Researchers have shown that SiO_2 and TiO_2 nanostructure can enhance the mechanical stability, surface morphology, wettability and rejection of the GO-based membranes. As can be seen in Table 2, there is a trade-off between water flux and rejection of membranes, and efforts for improving the rejection of GO membranes generally leads to a decrease in the water flux of these membranes, in which membranes exhibiting rejection higher than 90% show low water flux in the range of 9-218 $L \cdot m^{-2} \cdot h^{-1}$ [57,60,61]. The incorporation of the mentioned nanostructures between GO nanosheets can be achieved through ex-situ and in-situ hybridization approaches [62]. In ex-situ methods, GO and a pre-synthesized or commercially available nanostructure are mixed physically through electrostatic and π-π stacking interaction, so achieving uniform distribution of nanostructures on the GO nanosheets is very difficult to control. In contrast, the in-situ methods, such as hydrothermal and sol-gel methods, can provide uniform surface coverage by controlling the nucleation sites on GO nanosheets, while they consist of fewer steps and can provide a narrower size distribution of nanostructures. The size, shape, and the density of the nanostructures can be adjusted through altering the synthesis parameters to achieve more appropriate GO nanocomposites for the membrane separation processes [62]. In the current work, a one-step method was applied to prepare siloxane/GO membranes by pressure-assisted-self-assembly method of the as-synthesized siloxane/GOs using a dead-end cell. The insertion of siloxane network between the GO nanosheets led to a dramatic increase in the interlayer spacing of GO nanosheets, providing high pure water flux while maintaining high rejection (under a low operation pressure of 2.5 bar) toward cationic species of MB and neutral species of PG-P. The prepared siloxane/GO membranes also showed excellent stability under ultrasonication and were stable even after 60 min exposure to ultrasonic waves, while previously reported GO membrane just tolerated 30 min ultrasonication and collapsed afterward [63]. The siloxane/GO membranes also retained 95% of their rejection after chlorine attack test, implying their high chemical stability.

CONCLUSION

Siloxane/GO samples were synthesized by hydrolysis and condensation of TEOS in the presence of the GO nanosheets through a sol-gel process. The influence of altering synthesis parameters on the properties of the siloxane/GO samples was determined using various techniques. PES-supported thin film membranes were fabricated based on the unmodified GO, and the siloxane/GO samples and their separation performance, antifouling ability, chemical and mechanical stability were compared. Generally, the incorporation of siloxane network between GO nanosheets improved the structural, morphological, physicochemical features of the GO-based thin film membranes and their separation performance. The siloxane/GO samples appeared to have a larger interlayer spacing compared to the unmodified GO, due to the formation of covalent bonds between functional groups of GO and siloxane network. Larger siloxane network was formed in the siloxane/GO samples synthesized using a lower concentration of ammonium

hydroxide at higher temperature. The higher stability of the aqueous solution of the siloxane/GOs led to the formation of thin film membranes possessing smoother and denser surface morphology. Siloxane/GO membranes exhibited higher rejection ability for positively charged and neutral species compared to GO membranes. Moreover, the separation performance of siloxane/GO membranes was greatly affected by the size and surface charge of siloxane networks. These membranes represent promising antifouling properties and very high mechanical and chemical stability. Furthermore, the siloxane/GO thin film membranes containing larger siloxane network exhibited the highest FRR and R_r values, implying a higher flux recovery capacity and antifouling ability. The FRR value for membranes prepared based on the unmodified GO was about nine-times lower, while they showed the highest R_t and R_{ir} values owing to their rougher surface morphology. Results demonstrate that the modification of GO thin film by siloxane is an effective method to improve the separation performance, antifouling properties, chemical resistance and mechanical stability of GO-based thin film membranes, and that the siloxane/GO thin film membranes can be considered as promising candidate for different membrane separation applications by optimizing their preparation parameters.

ACKNOWLEDGEMENTS

The authors express their gratitude to Iran Nanotechnology Innovative Council (INIC) and the Analytical Chemistry laboratory in Amirkabir University of Technology, Tehran, Iran for all supports through this project.

CONFLICTS OF INTEREST

There are no conflicts of interest to declare.

SUPPORTING INFORMATION

Additional information as noted in the text. This information is available via the Internet at http://www.springer.com/chemistry/journal/11814.

REFERENCES

1. D. M. Warsinger, S. Chakraborty, E. W. Tow, M. H. Plumlee, C. Bellona, S. Loutatidou, L. Karimi, A. M. Mikelonis, A. Achilli, A. Ghassemi, L. P. Padhye, S. A. Snyder, S. Curcio, C. D. Vecitis, H. A. Arafat and J. H. Lienhard, *Prog. Polym. Sci.*, **81**, 209 (2018).
2. S. M. Hosseini, F. Karami, S. K. Farahani, S. Bandehali, J. Shen, E. Bagheripour and A. Seidypoor, *Korean J. Chem. Eng.*, **37**, 866 (2020).
3. O. Agboola, *Korean J. Chem. Eng.*, **36**, 1389 (2019).
4. Q. Bu, B. Wang, J. Huang, S. Deng and G. Yu, *J. Hazard. Mater.*, **262**, 189 (2013).
5. F. Tahmasebi, M. Alimohammadi, R. Nabizadeh, M. Khoobi, K. Karimian and A. Zarei, *Korean J. Chem. Eng.*, **36**, 894 (2019).
6. H. M. Hegab and L. Zou, *J. Membr. Sci.*, **484**, 95 (2015).
7. S. K. Srivastava and J. Pionteck, *J. Nanosci. Nanotechnol.*, **15**, 1984 (2015).
8. K. Krishnamoorthy, M. Veerapandian, K. Yun and S.-J. Kim, *Carbon*, **53**, 38 (2013).
9. Z. Jia and Y. Wang, *J. Mater. Chem. A*, **3**, 4405 (2015).
10. W.-S. Hung, C.-H. Tsou, M. De Guzman, Q.-F. An, Y.-L. Liu, Y.-M. Zhang, C.-C. Hu, K.-R. Lee and J.-Y. Lai, *Chem. Mater.*, **26**, 2983 (2014).
11. M. Hu and B. Mi, *Environ. Sci. Technol.*, **47**, 3715 (2013).
12. K. A. Mahmoud, B. Mansoor, A. Mansour and M. Khraisheh, *Desalination*, **356**, 208 (2015).
13. R. R. Nair, H. A. Wu, P. N. Jayaram, I. V. Grigorieva and A. K. Geim, *Science*, **335**, 442 (2012).
14. P. Sun, M. Zhu, K. Wang, M. Zhong, J. Wei, D. Wu, Z. Xu and H. Zhu, *ACS Nano*, **7**, 428 (2013).
15. Y. Li, S. Yuan, Y. Xia, W. Zhao, C. D. Easton, C. Selomulya and X. Zhang, *J. Membr. Sci.*, **601**, 117900 (2020).
16. H. Zhao, J. Yang, Z. Li, Y. Geng, J. Li, M. Chen, R. Li, Q. Li and L. Zhang, *J. Clean. Prod.*, **266**, 121884 (2020).
17. C. Xu, A. Cui, Y. Xu and X. Fu, *Carbon*, **62**, 465 (2013).
18. P. Sun, Q. Chen, X. Li, H. Liu, K. Wang, M. Zhong, J. Wei, D. Wu, R. Ma, T. Sasaki and H. Zhu, *NPG Asia Mater.*, **7**, e162 (2015).
19. M. Zhang, K. Guan, J. Shen, G. Liu, Y. Fan and W. Jin, *AIChE J.*, **63**, 5054 (2017).
20. H. Yang, N. Wang, L. Wang, H.-X. Liu, Q.-F. An and S. Ji, *J. Membr. Sci.*, **545**, 158 (2018).
21. Y. He, J. Wang, H. Zhang, T. Zhang, B. Zhang, S. Cao and J. Liu, *J. Mater. Chem. A*, **2**, 9548 (2014).
22. Y. Tian, Y. Cao, Y. Wang, W. Yang and J. Feng, *Adv. Mater.*, **25**, 2980 (2013).
23. S. Park, K.-S. Lee, G. Bozoklu, W. Cai, S. T. Nguyen and R. S. Ruoff, *ACS Nano*, **2**, 572 (2008).
24. Z. Jia, Y. Wang, W. Shi and J. Wang, *J. Membr. Sci.*, **520**, 139 (2016).
25. G. Wu, L. Ma, L. Liu, L. Chen and Y. Huang, *Thermochim. Acta*, **613**, 77 (2015).
26. W. Li, W. Liu, H. Wang and W. Lu, *J. Nanosci. Nanotechnol.*, **16**, 5734 (2016).
27. H. Wu, B. Tang and P. Wu, *J. Membr. Sci.*, **451**, 94 (2014).
28. S. Zheng and B. Mi, *Environ. Sci.: Water Res. Technol.*, **2**, 717 (2016).
29. Y.-H. Xi, J.-Q. Hu, Z. Liu, R. Xie, X.-J. Ju, W. Wang and L.-Y. Chu, *ACS Appl. Mater. Interfaces*, **8**, 15557 (2016).
30. A. Anand, B. Unnikrishnan, J.-Y. Mao, H.-J. Lin and C.-C. Huang, *Desalination*, **429**, 119 (2018).
31. W. S. Hummers and R. E. Offeman, *J. Am. Chem. Soc.*, **80**, 1339 (1958).
32. S. Valizadeh, M. H. Rasoulifard and M. S. S. Dorraji, *Appl. Surf. Sci.*, **319**, 358 (2014).
33. A. Kaniyoor and S. Ramaprabhu, *AIP Adv.*, **2**, 032183 (2012).
34. L. Jing-Feng, X. Zhen-Liang, Y. Hu, F. Cui-Ping and S. Jiang-Huan, *J. Appl. Polym. Sci.*, **107**, 4100 (2008).
35. J. Yin, G. Zhu and B. Deng, *Desalination*, **379**, 93 (2016).
36. D. Sioutopoulos, A. Karabelas and V. Mappas, *Membranes (Basel)*, **9**, 21 (2019).
37. S. Arefi-Oskoui, V. Vatanpour and A. Khataee, *J. Ind Eng. Chem.*, **41**, 23 (2016).
38. A. Shockravi, V. Vatanpour, Z. Najjar, S. Bahadori and A. Javadi, *Micropor. Mesopor. Mater.*, **246**, 24 (2017).

39. M. Sri Abirami Saraswathi, D. Rana, P. Vijayakumar, S. Alwarappan and A. Nagendran, *New J. Chem.*, **41**, 14315 (2017).
40. H. J. Kim, M.-Y. Lim, K. H. Jung, D.-G. Kim and J.-C. Lee, *J. Mater. Chem. A*, **3**, 6798 (2015).
41. J. Zha and H. Roggendorf, *Adv. Mater.*, **3**, 522 (1991).
42. L. P. Singh, S. K. Bhattacharyya, R. Kumar, G. Mishra, U. Sharma, G. Singh and S. Ahalawat, *Adv. Colloid Interface Sci.*, **214**, 17 (2014).
43. Y. Zhang, Y. Zhu, G. Lin, R. S. Ruoff, N. Hu, D. W. Schaefer and J. E. Mark, *Polymer*, **54**, 3605 (2013).
44. X. Zhou and T. Shi, *Appl. Surf. Sci.*, **259**, 566 (2012).
45. A. A. K. King, B. R. Davies, N. Noorbehesht, P. Newman, T. L. Church, A. T. Harris, J. M. Razal and A. I. Minett, *Sci. Rep.*, **6**, 19491 (2016).
46. S. Claramunt, A. Varea, D. López-Díaz, M. M. Velázquez, A. Cornet and A. Cirera, *J. Phys. Chem. C*, **119**, 10123 (2015).
47. S. Vollebregt, R. Ishihara, F. D. Tichelaar, Y. Hou and C. I. M. Beenakker, *Carbon*, **50**, 3542 (2012).
48. A. Sadezky, H. Muckenhuber, H. Grothe, R. Niessner and U. Pöschl, *Carbon*, **43**, 1731 (2005).
49. D. López-Díaz, M. López Holgado, J. L. García-Fierro and M. M. Velázquez, *J. Phys. Chem. C*, **121**, 20489 (2017).
50. Y. Li, *Probing the response of two-dimensional crystals by optical spectroscopy*, Springer International Publishing, Switzerland (2015).
51. P. S. Nerenberg and T. Head-Gordon, *Curr. Opin. Struct. Biol.*, **49**, 129 (2018).
52. Z. Fakharan, L. Naji and K. Madanipour, *J. Colloid Interface Sci.*, **540**, 272 (2019).
53. A. B. Bourlinos, D. Gournis, D. Petridis, T. Szabó, A. Szeri and I. Dékány, *Langmuir*, **19**, 6050 (2003).
54. V. Vatanpour, S. S. Madaeni, R. Moradian, S. Zinadini and B. Astinchap, *J. Membr. Sci.*, **375**, 284 (2011).
55. N. Akther, S. M. Ali, S. Phuntsho and H. Shon, *Desalination*, **491**, 114591 (2020).
56. P. Gao, Z. Liu, M. Tai, D. D. Sun and W. Ng, *Appl. Catal. B Environ.*, **138**, 17 (2013).
57. Y. Gao, M. Hu and B. Mi, *J. Membr. Sci.*, **455**, 349 (2014).
58. X. Yan, W. Tao, S. Cheng, C. Ma, Y. Zhang, Y. Sun and X. Kong, *Chemosphere*, **256**, 127118 (2020).
59. H. Lin, N. Mehra, Y. Li and J. Zhu, *J. Membr. Sci.*, **593**, 117401 (2020).
60. X. Chen, M. Qiu, H. Ding, K. Fu and Y. Fan, *Nanoscale*, **8**, 5696 (2016).
61. G. Zeng, Y. He, Z. Ye, X. Yang, X. Chen, J. Ma and F. Li, *Ind. Eng. Chem. Res.*, **56**, 10472 (2017).
62. S. Mitra, S. Banerjee, A. Datta and D. Chakravorty, *Condensed Matter*, arXiv:1207.1995 (2012)
63. J. Hou, C. Bao, S. Qu, X. Hu, S. Nair and Y. Chen, *Appl. Surf. Sci.*, **459**, 185 (2018).